Absolute quantum yield of short-wave infrared luminescence of $GdVO_4$: Yb^{3+}, Er^{3+}, Zn^{2+} nano- and microparticles

Yupaporn Niyom [a], Eduard Madirov [c], Nisrin Mohamed Bhiri [c], Aditya Chauhan [c], Bryce S. Richards [c], Adrian Flood [a], Daniel Crespy [b], Andrey Turshatov [c,*]

[a] Department of Chemical and Biomolecular Engineering, School of Energy Science and Engineering, Vidyasirimedhi Institute of Science and Technology (VISTEC), Rayong, 21210, Thailand

[b] Department of Materials Science and Engineering, School of Molecular Science and Engineering, Vidyasirimedhi Institute of Science and Technology (VISTEC), Rayong, 21210, Thailand

[c] Institute of Microstructure Technology, Karlsruhe Institute of Technology, Hermann-von-Helmholtz-Platz 1, 76344, Eggenstein-Leopoldshafen, Germany

Keywords:
$GdVO_4$
Quantum yield
Photoluminescence
Nanoparticle
Infrared luminescence

A B S T R A C T

Orthovanadate ($GdVO_4$) nano- and microparticles doped with lanthanide ions are of interest for anti-counterfeiting and plastics recycling applications due to their emission in the short-wave infrared (SWIR) region. The unique aspect of this study is the measurement of the absolute photoluminescence quantum yield (QY) of the SWIR (1533 nm) emission for the orthovanadate nano- and microparticles co-doped withF Yb^{3+} and Er^{3+} using an integrating sphere. This is the first demonstration that doping with optically neutral Zn^{2+} ion significantly improves the QY of SWIR emission. A low QY of 0.1% was observed for the $GdVO_4$:Yb^{3+}, Er^{3+}, Zn^{2+} nanoparticles synthesized by the co-precipitation method. However, the QY can be significantly increased (QY of 27.2%) after a 700 °C calcination step. This performance is approximately double that of a reference phosphor – Zn^{2+}-free $GdVO_4$:Yb^{3+},Er^{3+} synthesized by solid-phase reaction at 1050 °C – which achieved only QY of 13.0%. When micron-sized $GdVO_4$:Yb^{3+}, Er^{3+}, Zn^{2+} particles are dispersed in water, a decrease in QY was observed (2.3%), which is explained by reabsorption of the luminescence by water. However, the water environment strongly quenched the SWIR luminescence (QY < 0.1%) in case of $GdVO_4$:Yb^{3+}, Er^{3+}, Zn^{2+} nanoparticles with size of 125 nm. In summary, $GdVO_4$:Yb^{3+}, Er^{3+}, Zn^{2+} microparticles with a QY of 27.2% can be used as bright luminescent markers in an advanced plastics processing technology - tracer-based sorting.

1. Introduction

Optical transparency windows in the near-infrared (NIR, 700–1000 nm) and shortwave infrared (SWIR, 1000–2400 nm) regions are important phenomena for applications in many, sometimes not obviously related practical fields. For example, by reducing absorption and scattering, phosphors emitting in this spectral region can provide exceptional depth of light penetration and the associated effectiveness of *in vivo* optical imaging technologies in clinical practice and biomedical research [1,2]. More generally, the same phosphors can be used as anti-counterfeiting inks [3] or as markers to improve quality of plastics recycling using a tracer-based sorting process [4,5]. To better understand the latter application, it should be noted that state-of-the-art plastics recycling technology uses measurements of the spectral differences between the reflectance spectra of different polymers in the NIR-SWIR range [6]. For this purpose, the sorting machine is equipped with a halogen lamp and an InGaAs detector (to measure spectra in the range of 900–1700 nm). This means that, when NIR-SWIR luminescent phosphors are used as markers, labelled objects can be effectively identified with the same InGaAs detector. This makes it possible to separate objects made from the same polymer but with different degrees of purity or from different manufacturers. This high level of polymer separation is unattainable with current technology, so the use of NIR-SWIR luminescent markers can be a great idea for the recycling of plastic materials.

Several luminophores can be considered as potential agents for NIR-SWIR applications. These include dyes [7], single-walled carbon nanotubes [2], quantum dots [2], nanoparticles exhibiting aggregation-induced emission (AIE) [8–10] or conjugated polymers of the donor–acceptor type [11]. Another attractive example of

* Corresponding author.
E-mail address: andrey.turshatov@kit.edu (A. Turshatov).

NIR-SWIR-active luminophores are inorganic nanocrystals or microcrystals co-doped with lanthanide ions, such as Er^{3+}, Nd^{3+}, Ho^{3+} and Tm^{3+} [12,13], which are suitable for luminescent applications due to their high photostability and long luminescence lifetime.

Over the last decade, orthovanadate-(VO_4^3)-based materials co-doped with lanthanide ions have been investigated for many applications, including lasers [14], oxidant sensors, magnetic resonance imaging (MRI) contrast agents, and optical imaging in the visible range [15–20]. However, much less is known about their NIR-SWIR properties. Often the luminescence quantum yield is not described, although this parameter is very useful for comparing different luminophores and for studying the influence of the environment on the luminescence intensity.

In general, orthovanadate-based phosphors with micron-sized particles can be synthesized using a conventional high temperature (1050 °C) solid-state synthesis [21]. Three other methods for the synthesis of multifunctional orthovanadate nanoparticles can also be identified: (i) the citrate method, also known as the modified Pechini method; (ii) hydrothermal synthesis; and (iii) co-precipitation. The first two methods – resulting in particle sizes of 10–15 nm for (i) [22] and 40–80 nm for (ii) [23–25] – are widely used for the synthesis of MRI contrast agents and visible-emitting phosphors (co-doped with Eu^{3+}). These materials typically do not require additional calcination at elevated temperatures (>500 °C). However, it has been reported that the intensity of the Eu^{3+}-based red emission can be significantly improved after high temperature treatment (in the range 500–900 °C) [26–28]. In contrast, lanthanide-doped materials active in the NIR and SWIR ranges require calcination (>500 °C) to reduce the strong quenching of the corresponding excited states (e.g. the $^4I_{11/2}$ and $^4I_{13/2}$ states for Er^{3+}) [29–31]. These nanoparticles are often relatively large (>100 nm) and are obtained by the co-precipitation method.

In our previous study, $GdVO_4$:Yb^{3+}, Er^{3+}, Zn^{2+} nanoparticles prepared by co-precipitation followed by high temperature calcination at 850 °C were shown to enhance the upconversion luminescence of the nanoparticles. This was attributed to the increase in particle size from ~100 nm to ~2 μm and the crystal lattice shrinkage induced by Zn^{2+} [21]. In this work, the synthesis conditions of orthovanadate ($GdVO_4$:Yb^{3+}, Er^{3+} and $GdVO_4$:Yb^{3+}, Er^{3+}, Zn^{2+}) nano- and microparticles are investigated together with the effect on the SWIR emission of Er^{3+} (with peak luminescence at 1530 nm). The $GdVO_4$-based phosphors were mostly synthesized by the co-precipitation method, with one sample also prepared by high-temperature solid-phase reaction. The latter served as a reference sample with high photoluminescence QY, while the co-precipitation method was investigated as a suitable approach for the production of nanoparticles. The lack of knowledge about the QY of SWIR emission in $GdVO_4$-based particles led to the study of the relationship between QY and synthesis conditions, as well as the influence of the environment on the QY and luminescence lifetime. The QY values were determined for both dry powders and aqueous dispersions using an absolute method (in an integrating sphere). The QY values obtained also serve as a basis for further optimization of NIR-SWIR markers for plastics recycling.

2. Experimental section

2.1. Materials

Gadolinium (III) nitrate hexahydrate ($Gd(NO_3)_3{\cdot}6H_2O$, ≥99.9%, Sigma-Aldrich), ytterbium (III) nitrate hexahydrate ($Yb(NO_3)_3{\cdot}6H_2O$, ≥99.9%, Sigma-Aldrich), erbium (III) nitrate hexahydrate ($Er(NO_3)_3{\cdot}6H_2O$, ≥99.9%, Sigma-Aldrich), zinc(II) nitrate hexahydrate ($Zn(NO_3)_2{\cdot}6H_2O$, ≥99.9%, Sigma-Aldrich), gadolinium (III) oxide (Gd_2O_3, ChemPur, 99.9%), ytterbium (III) oxide (Yb_2O_3, ChemPur, 99.9%), erbium (III) oxide (Er_2O_3, ChemPur, 99.9%), polyvinylpyrrolidone (PVP, M_w ~40,000 g mol ^{1}, Sigma-Aldrich), ammonium metavanadate (NH_4VO_3, ≥99.0%, Sigma-Aldrich) and sodium orthovanadate (Na_3VO_4, ≥99.9%, Acros Organics) were used as received. Deionized water was used in all experiments.

2.2. Synthesis of $GdVO_4$:Yb^{3+},Er^{3+} microparticles

For comparative analysis, reference $GdVO_4$:Yb^{3+},Er^{3+} microparticles were prepared using a solid-phase reaction technique. Typically, all oxides (Gd_2O_3, Yb_2O_3, and Er_2O_3) were weighed in stoichiometric ratio with 5% excess ammonium metavanadate (NH_4VO_3) and ground together using a mortar and pestle for 15 min. The ground powders were then transferred to covered alumina crucibles and calcined in air at 1050 °C (with a ramp rate of 5 °C/min) for 2 h in a muffle furnace (KLS 05/11, Thermconcept). The calcined powders were repeatedly washed with dilute NaOH solution (0.1 M) until all unreacted vanadium pentoxide (formed after the decomposition of ammonium metavanadate) was removed, as evidenced by the colour change of the phosphor from yellow to white. The washed powders were dried overnight at 80 °C in a vacuum oven.

2.3. Synthesis of $GdVO_4$:Yb^{3+},Er^{3+} and $GdVO_4$:Yb^{3+},Er^{3+},Zn^{2+} nanoparticles

$GdVO_4$:Yb^{3+},Er^{3+} nanoparticles were synthesized by the co-precipitation method [21]. An aqueous solution was prepared by dissolving $Gd(NO_3)_3$ (2.275 g), $Yb(NO_3)_3$ (0.377 g), $Er(NO_3)_3$ (0.053 g), and PVP (3 g) separately in deionized water (150 ml). Meanwhile, Na_3VO_4 (1.104 g) was dissolved in deionized water (150 ml). The aqueous Na_3VO_4 solution was added dropwise into the metal-nitrate solution. The mixtures were then stirred at 500 rpm for 30 min to obtain white precipitates. The product was collected by centrifugation at 6000 rpm for 6 min and washed three times with deionized water and ethanol. The purified product was dried at 60 °C for 24 h and then ground with a mortar and pestle to obtain a fine powder. The samples were then calcined at 700 °C (with a ramp rate of 5 °C/min) for a variable time using a bottom loading furnace (BLF1700, Carbolite). Finally, the calcined samples were ground with a mortar and pestle, and stored in polystyrene cuvettes for further characterization. A similar procedure was followed for $GdVO_4$:Yb^{3+}, Er^{3+}, Zn^{2+} nanoparticles. In this synthesis, additional $Zn(NO_3)_2$ (0.26 g) was dissolved in the metal-nitrate solution (150 ml).

2.4. Analytical tools

The hydrodynamic diameter and polydispersity index (PDI) of the nanoparticles were measured at 25 °C using dynamic light scattering (DLS) with a laser wavelength of 658 nm at an angle of 165° on a Litesizer 500 (Anton Paar GmbH). The morphology of the powder nanoparticles was observed by scanning electron microscopy (SEM) (Zeiss Supra 60VP). The X-ray powder diffraction (XRPD) was performed using a D2 Phaser system (Bruker) with a monochromatic Cu Kα radiation (λ = 1.54 A°) at 30 kV with a current of 10 mA. Data were acquired between 2Θ angles of 10° and 80° with a dwell time of 1 s and a step size of 0.02°. The crystallite size was calculated from the Scherrer equation for the maximum intensity reflection $2\Theta = 24.6°$ [200] using the Gaussian function.

Diffuse reflectance (DRS) and absorbance spectra were obtained using a UV/Vis/NIR spectrophotometer (Lambda 950, PerkinElmer). The Fourier-transform infrared (FTIR) spectroscopy was performed using a spectrometer (Vertex 70, Bruker) equipped with an attenuated total reflection (ATR) sample holder.

The decay curves of the excited states of Er^{3+} and Yb^{3+} ions were obtained using an infrared single-photon detector (ID Quantique, ID220) coupled to a double monochromator (Bentham, DTMS300). The sample was excited with a 976 nm continuous-wave (CW) laser diode (Thorlabs, L980P200) modulated using the built-in functionality of the laser diode controller (Thorlabs, ITC4001) with a 70 ms duration and 20

ms pulse width for the Er^{3+} emission and a 15 ms duration and 5 ms pulse width for the Yb^{3+} emission. The trigger signal is fed to the multichannel scaling card (PicoQuant, TimeHarp 260) after being delayed by 20 μs using a custom-built Arduino-based delay generator.

The Raman spectrum for the undoped $GdVO_4$ sample was recorded using 785 nm excitation with an i-Raman setup (Polytec).

2.5. Determination of quantum yield

The photoluminescence QY value is a metric that is defined as the ratio of the number of photons emitted to the number of photons absorbed by a sample. The QY value was evaluated using an optical setup with an integrating sphere. The sample was placed in the center of an integrating sphere (Labsphere, 6″ Ø, 3 P-LPM-060-SL) and was excited by a CW laser diode operating at 976 nm (Thorlabs, L980P200). The laser diode was mounted on a temperature-controlled mount (Thorlabs, TCLDM9) and driven by a laser diode controller (Thorlabs, ITC4001). The QY of the Er^{3+} emission band centred around 1550 nm was calculated by using the so-called 3 M method [32] as described in Eq. (1).

$$QY = \frac{PD \quad PI\frac{LD}{LI}}{ES\left(1 \quad \frac{LD}{LI}\right)} \tag{1}$$

Here *PD* is the emission intensity of the sample when it is directly hit by the excitation laser; *PI* is the emission intensity of the sample when it is placed inside the integrating sphere but out of the path of the excitation laser, so that it is only excited by the scattered laser light; *LD* is the intensity of the excitation laser inside the integrating sphere when it hits the sample directly; *LI* is the intensity of the excitation laser when the sample is placed inside the integrating sphere but out of the path of the laser and *ES* is the intensity of the excitation laser in the empty sphere.

A spectrometer (NIRQuest, Ocean Insight) was used to detect both the emission spectrum of the sample and the intensity of the excitation laser. To filter the excitation wavelength from the analysis, a 980 nm long pass filter (Semrock, LP02-980RE-25) was placed between the output port of the integrating sphere and the collecting optical fibre. The spectrometer was calibrated for intensity together with the integrating sphere using a calibration lamp (HL-3plus-INT-CAL-EXT, Ocean Insight). A quartz wedge (reflection = 4%) was used to reflect a fraction of the laser beam onto a Si photodiode power sensor (S121C, Thorlabs). The power of the excitation laser was monitored with a power meter (Thorlabs, PM320E). The beam size was determined using a beam profiler (Thorlabs, BP209-IR/M) and using a 2σ definition for the semi-minor and semi-major axes, the area of the beam is calculated to be 61.7×10^{-3} cm^2.

To obtain the intensity-dependent QY the same setup and measurement techniques were used at each excitation intensity. The power of the incident laser light was varied using a neutral density (ND) filter wheel (Thorlabs, NDC-100C-2) attached to a stepper motor. The whole system was automated and controlled by a custom developed software using the LabView environment.

The QY values were obtained for three conditions: dry powder, powder dispersed in H_2O (10 mg of particles in 1 ml of H_2O) and powder dispersed in D_2O (10 mg of particles in 1 ml of D_2O). It should be noted that there is a significant overestimation of the number of photons absorbed in the case of the sample dispersed in H_2O due to the strong water absorption at 980 nm. To correct the overestimated parameter, the absorption of $GdVO_4$:Yb^{3+},Er^{3+},Zn^{2+} measured for the dispersion in D_2O (without solvent absorption) was used for the calculation of QY with Eq. (1).

3. Results

Two synthetic methods were used in this work: (i) high-temperature solid-phase reaction; (ii) co-precipitation method. The as-precipitated sample was also calcined at 700 °C.

3.1. Samples prepared by co-precipitation method

The QY of the Er^{3+}:$^4I_{13/2}$ emission (1533 nm) for dry powder of $GdVO_4$:Yb^{3+},Er^{3+} nanoparticles was observed to be very low (0.02%). To enhance the luminescence, the nanoparticles were calcined at 700 °C for different time periods (2, 4, 6, 8, and 24 h). High-temperature calcination resulted in a significant increase in QY for the SWIR emission of the Er^{3+}:$^4I_{13/2}$ state (Fig. 1a and S1). After 2 h of calcination, the solid state QY increased up to 2.2% and then increased steadily with increasing calcination time to reach 3.5% after 24 h of calcination. It should be noted that only 976 nm excitation and SWIR luminescence in the range of 1450–1650 nm was used to calculate QY for all samples in this manuscript.

There are several possible reasons to explain the poor QY prior to high-temperature calcination. The XRD patterns of as-prepared $GdVO_4$:Yb^{3+},Er^{3+} (Fig. 1b) suggest a very small crystallite size (7 nm), which increases to 15 nm (2 h of calcination) and 19 nm (24 h of calcination) (Table S1). The small crystallite size in the uncalcined sample could lead to the formation of many grains, creating quenching centers such as grain boundary defects. The number of interfacial quenching centers decreased after calcination, resulting in an increase of luminescence.

However, the poor crystallinity was probably not the dominant reason for the lack of strong luminescence. For example, $GdVO_4$ nanoparticles co-doped with Eu^{3+} exhibited relatively efficient visible luminescence without high-temperature calcination [33]. Thus, it was suggested that another type of quenching center – hydroxyl groups – was responsible for quenching either the Er^{3+}:$^4I_{13/2}$ state or the Er^{3+}:$^4I_{11/2}$&Yb^{3+}:$^4F_{5/2}$ manifold. FTIR spectra (Fig. 1c) indicate the presence of –OH groups as characteristic broad signals at 3300 cm^{-1} (with a full width half maximum of ~500 cm^{-1}), corresponding to the fundamental frequency of the stretching vibration. The fundamental vibration is resonant with the energy gap (3565 cm^{-1}) between Er^{3+}:$^4I_{11/2}$ and Er^{3+}:$^4I_{13/2}$ states resulting in efficient quenching of the Er^{3+}:$^4I_{11/2}$&Yb^{3+}:$^4F_{5/2}$ manifold. Furthermore, the first overtone of the –OH stretching vibration is resonant with the energy gap (6535 cm^{-1}) between the Er^{3+}:$^4I_{13/2}$ state and the ground (Er^{3+}:$^4I_{15/2}$) state. Although, the quenching of the Er^{3+}:$^4I_{13/2}$ state is less likely due to the slower rate of two-phonon relaxation (by the first overtone) as compared to single-phonon relaxation (by the fundamental vibration frequency), it can still compete with the rate of radiative decay [34,35]. Fig. 1c demonstrates that the FTIR signal corresponding to –OH groups decreased during calcination, resulting in a decrease in the quenching rate and an increase in QY. However, a complete removal of –OH groups was not achieved even after 24 h of calcination at 700 °C.

In the absence of –OH quenching centers, the SWIR luminescence efficiency in $GdVO_4$ is influenced by the maximum phonon energy, which can be obtained from the Raman spectrum (Fig. 1d). The Raman signal at 884 cm^{-1}, corresponding to the maximum phonon energy, has an energy that was insufficient to bridge the energy gap of the Er^{3+}:$^4I_{13/2}$ state (1530 nm, 6535 cm^{-1}) with a reasonable number of phonons (5–6 phonons).

There is a traditional way to obtain good luminescent materials without many defects and quenching sites – the high-temperature solid-phase method. Therefore, it was interesting to compare $GdVO_4$:Yb^{3+},Er^{3+} prepared by co-precipitation reaction and calcined at 700 °C with a reference sample prepared by traditional solid-phase method [21].

3.2. Sample prepared by solid-phase synthesis

Fig. 2a displays the XRD pattern of the $GdVO_4$:Yb^{3+},Er^{3+}(sp) sample synthesized by a high-temperature (1050 °C) solid-phase reaction. This pattern corresponds to the tetragonal Gd-orthovanadate (JCPDS Card No. 170260) with the crystallite size of 88 nm. Microparticles 1–4 μm in size were observed in the solid-phase reaction product by SEM imaging

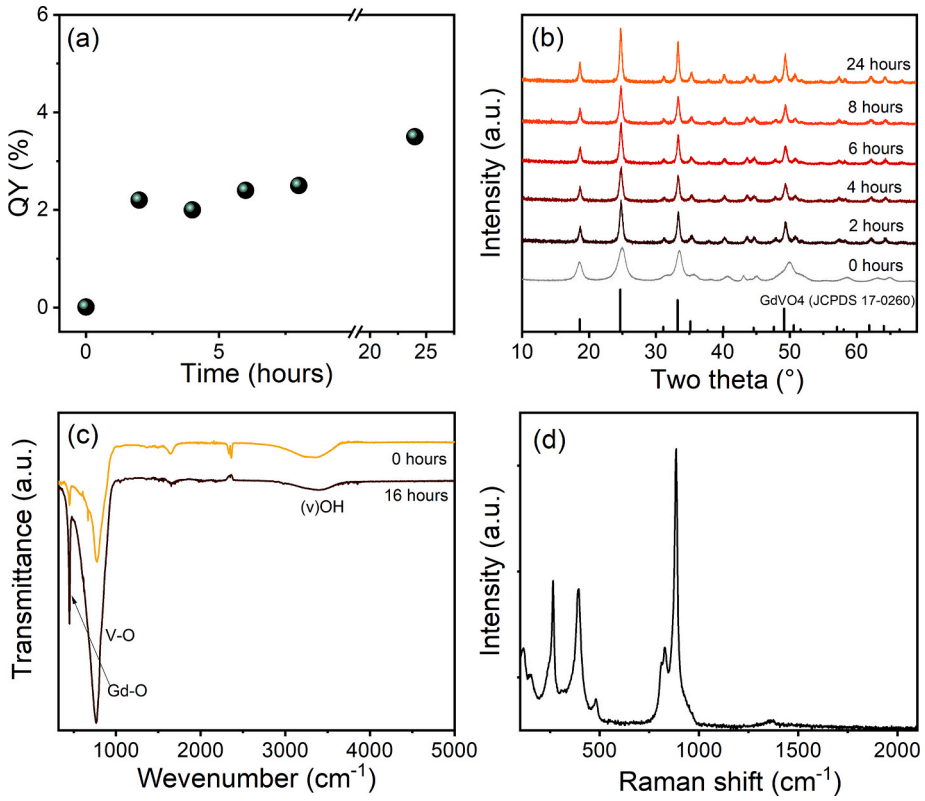

Fig. 1. (a) QY of 1533 nm emission in $GdVO_4:Yb^{3+},Er^{3+}$ solid samples calcined at 700 °C for different times. The samples were excited by a 976 nm laser (1 W/cm^2); (b) XRD data of $GdVO_4:Yb^{3+}$, Er^{3+} samples calcined at 700 °C; (c) FTIR spectra of $GdVO_4:Yb^{3+},Er^{3+}$ sample before calcination and after 24 h calcination at 700 °C; (d) Raman spectra of $GdVO_4:Yb^{3+}$ sample by 785 nm laser. All samples were synthesized by the co-precipitation method.

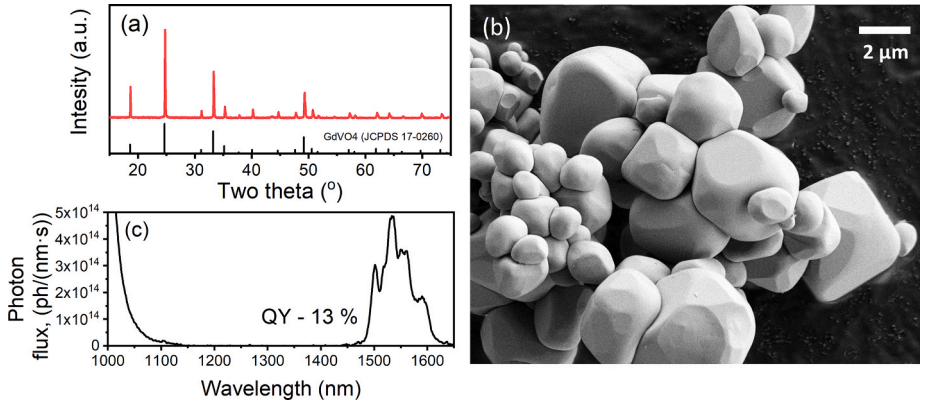

Fig. 2. (a) XRD data of $GdVO_4:Yb^{3+}$, Er^{3+}(sp) sample prepared by high-temperature solid state reaction; (b) representative SEM images for a $GdVO_4:Yb^{3+}$, Er^{3+}(sp) sample; (c) SWIR emission for $GdVO_4:Yb^{3+}$, Er^{3+}(sp) sample excited by 976 nm laser (excitation intensity of 1 W/cm^2). The $GdVO_4:Yb^{3+}$, Er^{3+}(sp) sample is co-doped with 2 mol % Yb^{3+} and 12 mol % Er^{3+}.

(Fig. 2b). Excitation of the $GdVO_4:Yb^{3+},Er^{3+}$(sp) sample with a 976 nm laser resulted in SWIR luminescence of the $Er^{3+}:{}^4I_{13/2}$ state with the peak at 1533 nm as well as luminescence at $\lambda < 1100$ nm corresponding to the emission of the $Yb^{3+}:{}^4F_{5/2}$ state (Fig. 2c). The incomplete energy transfer from the $Yb^{3+}:{}^4F_{5/2}$ state to the $Er^{3+}:{}^4I_{13/2}$ state can be explained by the very close energy of these states and, consequently, by the possibility of backward energy transfer ($Er^{3+}:{}^4I_{13/2} \rightarrow Yb^{3+}:{}^4F_{5/2}$) [36]. Despite the incomplete energy transfer, the absolute QY of $Er^{3+}:{}^4I_{13/2}$ emission in dry powder measured in an integrating sphere was high (13.0%), probably due to the absence of –OH quenching centers, as confirmed by FTIR data (Fig. S2).

It has been demonstrated that the co-doping of $GdVO_4:Yb^{3+},Er^{3+}$ with Zn^{2+} results in an upconversion QY that exceeds the QY of the $GdVO_4:Yb^{3+},Er^{3+}$ microparticles prepared by the solid-state reaction [21]. Therefore, the investigation of the effect of Zn^{2+} on the QY luminescence of the $Er^{3+}:{}^4I_{13/2}$ state in samples synthesized by the co-precipitation method was continued.

3.3. *Samples prepared via co-precipitation method in presence of Zn^{2+}*

Although the $GdVO_4:Yb^{3+},Er^{3+},Zn^{2+}$ nanoparticles synthesized by the co-precipitation method exhibited a very low QY of 0.1% for 1533 nm emission in the solid state, a very strong increase in QY up to 27.2% was achieved after 24 h of calcination at 700 °C (Fig. 3a). It should be noted that QY values for Er^{3+} SWIR emission measured with an integrating sphere are rather scarce in the literature. Several publications

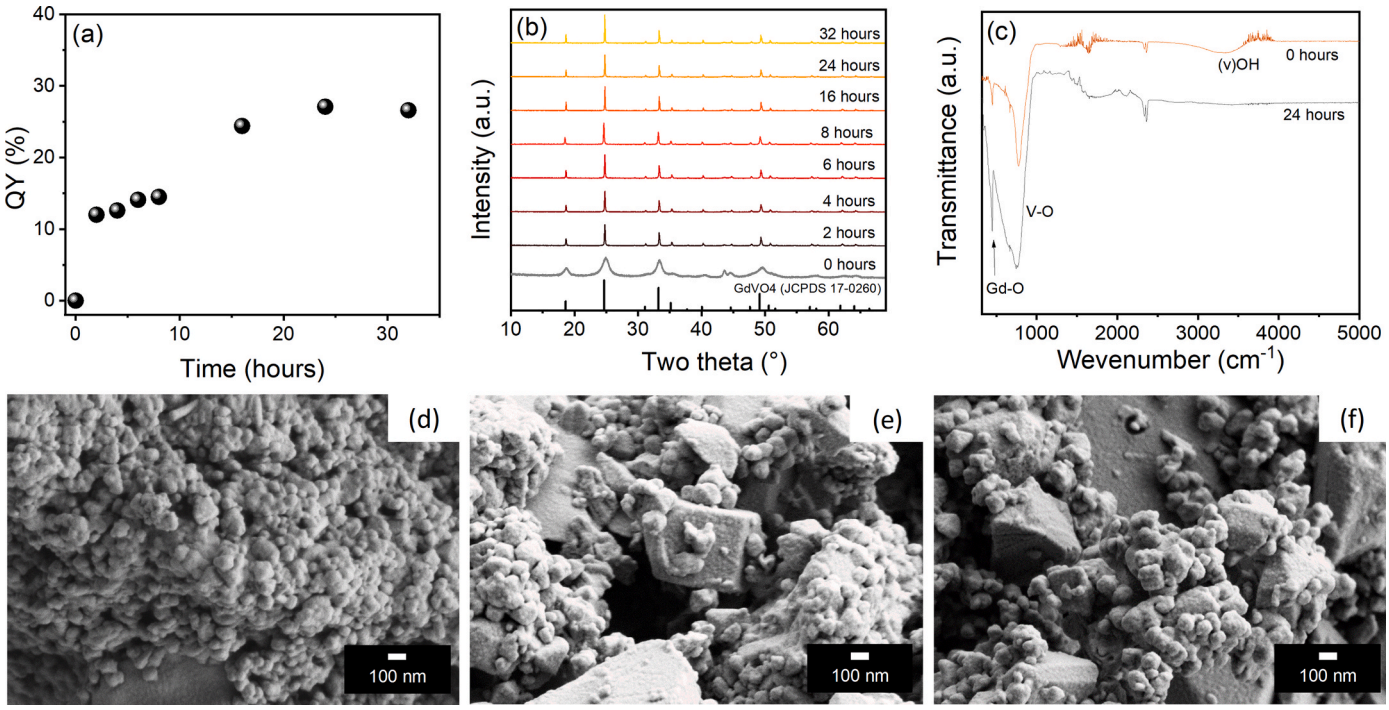

Fig. 3. (a) QY of 1533 nm emission in $GdVO_4$:Yb^{3+},Er^{3+},Zn^{2+} solid samples calcined at 700 °C for different times. The samples were excited by 976 nm laser (1 W/cm^2); (b) XRD data of $GdVO_4$:Yb^{3+},Er^{3+},Zn^{2+} samples calcined at 700 °C for different times; (c) FTIR spectra of $GdVO_4$:Yb^{3+},Er^{3+},Zn^{2+} samples before calcination and after 16 h calcination at 700 °C; (d–f) representative SEM images for $GdVO_4$:Yb^{3+},Er^{3+},Zn^{2+} samples calcined at 700 °C for 2 h (d), 16 h (e), and 24 h (f). All $GdVO_4$:Yb^{3+},Er^{3+},Zn^{2+} samples were synthesized by the co-precipitation method.

have reported very high QY (up to 100% for Er^{3+} doped $LaPO_4$) [37] where QY was determined as the ratio between the decay time (experimental value) and the calculated radiative lifetime [38,39]. Later, QY of SWIR Er^{3+} emission measured for series of perovskite and CaS crystals using an integrating sphere resulted in lower values, the QY range being 4.3–9.3% [40–42].

Comparison of XRD patterns showed an increase in crystallite size for samples prepared with Zn^{2+} (71 nm after 24 h of calcination, Table S2) compared to samples prepared without Zn^{2+} (19 nm after 24 h of calcination, Table S1). The effect of reducing the number of defects at grain boundaries could lead to a higher QY. A disappearance of –OH groups was observed for the sample prepared in the presence of Zn^{2+}, as shown in Fig. 3c, where the signal at 3300 cm ^{1} was not observed. Thus, the absence of quenching centers (-OH groups) hence also contributed to an increase in QY.

The modification of the crystal structure of $GdVO_4$ with the inclusion of Zn^{2+} ions further improved the optical performance. For example, the QY of the $GdVO_4$:Yb^{3+},Er^{3+},Zn^{2+} sample (27.2%) was almost twice as high as compared to that of the $GdVO_4$:Yb^{3+},Er^{3+}(sp) reference sample (13.0%). Note that the reference sample has the same crystallite size and lack of –OH group as the $GdVO_4$:Yb^{3+},Er^{3+},Zn^{2+} sample. Thus, the improvement in optical properties in the presence of Zn^{2+} can be explained by the smaller radius of Zn^{2+} (90 p.m.) than the host Gd^{3+} ion (105 p.m.) and the different valence of Zn^{2+}. Therefore, the incorporation of Zn^{2+} as a substitutional dopant at Gd^{3+} sites leads to a significant reduction in cell volume and cell symmetry, resulting in an enhancement of the radiative transition in Yb^{3+} and Er^{3+}. To test this hypothesis, we synthesized samples co-doped with Yb^{3+}, namely $GdVO_4$:Yb^{3+} and $GdVO_4$:Yb^{3+},Zn^{2+}, and measured the decay time and PLQY for the emission $^2F_{5/2} \rightarrow {}^2F_{7/2}$ (Fig. S3). Since Yb^{3+} has only one excited state $^2F_{3/2}$, it can be assumed that the decay time, the PLQY and the radiative lifetime are related to each other as follows

$$PLQY = \frac{\tau}{\tau_{rad}} \quad (2)$$

The results of Fig. S3 show that the radiative lifetime of the Yb^{3+} luminescence decreases from 1.06 ms to 0.48 ms for $GdVO_4$:Yb^{3+} and $GdVO_4$:Yb^{3+},Zn^{2+} samples, respectively, which supports our idea about the enhancement of the radiative transition upon co-doping with Zn^{2+}.

Furthermore, the change in particle size during calcination of samples synthesized by the co-precipitation method was investigated. In the case of $GdVO_4$:Yb^{3+},Er^{3+},Zn^{2+}, the co-precipitation method led to the formation of relatively small nanoparticles with a size of 71 nm (Fig. 4a) with a very low QY of 0.1% (measured for the dried sample). On the other hand, after 2 h of calcination at temperature of 700 °C, the QY value increased up to 12.2%. However, a bimodal size distribution was observed in the volume-weighted size distribution of size obtained by DLS. Since the volume-weighted distribution provides information about the mass fraction of particles with the corresponding diameter, assuming that small and large particles have a similar density, the DLS data indicated the simultaneous presence of a significant weight amount (~70 wt%) of large particles with sizes of ~400 nm and a fraction of ~30 wt% of small nanoparticles (84 nm). Longer calcination resulted in the simultaneous formation of microparticles and nanoparticles with sizes of 107 nm (after 8 h calcination) and 136 nm (after 24 h calcination). At the same time, the QY increased up to 14.8% and 27.2%, respectively. Although DLS method should be applied with some degree of caution to micron-sized particles with complex shapes, the DLS results were consistent with the SEM images shown in Fig. 3d–f. In fact, the SEM images also exhibited the presence of large microcrystals after 12 and 24 h of high-temperature calcination.

Given the bimodal size distribution in the $GdVO_4$:Yb^{3+},Er^{3+},Zn^{2+} samples, the question arose whether the observed high QY value measured for the solid sample was imparted to both large (micrometer scale) and small (nanometer scale) particles. To answer this question, a sample of $GdVO_4$:Yb^{3+},Er^{3+},Zn^{2+} prepared after 16 h of calcination and a QY of 24.5% was dispersed in water. After 48 h, large particles were sedimented and only small nanoparticles with an average size of 125 nm were observed in the suspension (Fig. 4b). The aqueous dispersion was carefully separated from the precipitate and dried before measuring the

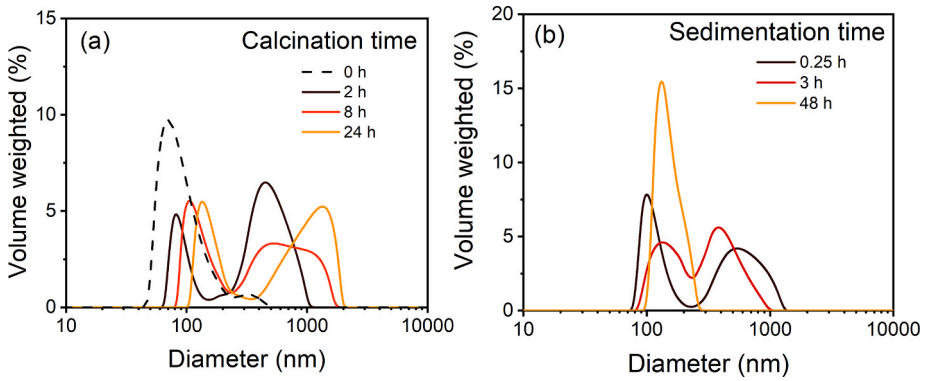

Fig. 4. DLS data for (a) $GdVO_4$:Yb^{3+},Er^{3+},Zn^{2+} sample before calcination and after calcination at 700 °C; (b) $GdVO_4$:Yb^{3+},Er^{3+},Zn^{2+} (16 h) sample after the sedimentation process.

QY for the emission from the Er^{3+}:$^4I_{13/2}$ state. The resulting fraction of small particles had a relatively low QY value of 0.9% (measured for the dried sample). To elucidate the origin of the size-dependent luminescence of $GdVO_4$:Yb^{3+},Er^{3+},Zn^{2+} particles, the lifetimes of the Er^{3+}:$^4I_{13/2}$ state (1533 nm emission) and the Er^{3+}:$^4I_{11/2}$&Yb^{3+}:$^4F_{5/2}$ manifold (1010 nm emission) were measured for two solid samples (Fig. 5a and b). Since radiative and non-radiative transitions involving these states determine the quantum yield of the SWIR radiation, the lifetime behavior can shed light on the cause of luminescence quenching. The measurements were carried out on a sample of $GdVO_4$:Yb^{3+},Er^{3+},Zn^{2+}(16 h) (consisting of a mixture of microparticles and nanoparticles) and on a fraction containing only nanoparticles $GdVO_4$:Yb^{3+},Er^{3+},Zn^{2+}(np) obtained after the sedimentation process of the aforementioned $GdVO_4$:Yb^{3+},Er^{3+},Zn^{2+}(16 h) sample. As shown in Fig. 5a, there was no significant difference between the lifetime of the Er^{3+}:$^4I_{13/2}$ state for two samples. However, the lifetime of the Er^{3+}:$^4I_{11/2}$&Yb^{3+}:$^4F_{5/2}$ manifold (Fig. 5b) was much shorter for the nanoparticle fraction (0.07 ms) as compared with the $GdVO_4$:Yb^{3+},Er^{3+},Zn^{2+}(16 h) sample (0.12 ms).

At the same time, the FTIR spectrum obtained from the $GdVO_4$:Yb^{3+},Er^{3+},Zn^{2+}(np) sample (Fig. S4) shows a clear signature corresponding to –OH groups. This result revealed that –OH quenching centers appeared on the surface as soon as the dried nanoparticles were placed in water and can not removed by the subsequent drying at 80 °C. Therefore, the reduced QY for the $GdVO_4$:Yb^{3+},Er^{3+},Zn^{2+}(np) sample was mainly related to the presence of quenching centers (–OH–groups) on the particle surface and their influence on the lifetime of the Er^{3+}:$^4I_{11/2}$&Yb^{3+}:$^4F_{5/2}$ manifold, but not to the small particle size. The shorter lifetime of the Er^{3+}:$^4I_{11/2}$&Yb^{3+}:$^4F_{5/2}$ manifold reduced both the energy transfer probability from Yb^{3+} to Er^{3+} and the transition probability from Er^{3+}:$^4I_{11/2}$ to Er^{3+}:$^4I_{13/2}$, thereby decreasing the QY of the Er^{3+}:$^4I_{13/2}$ state.

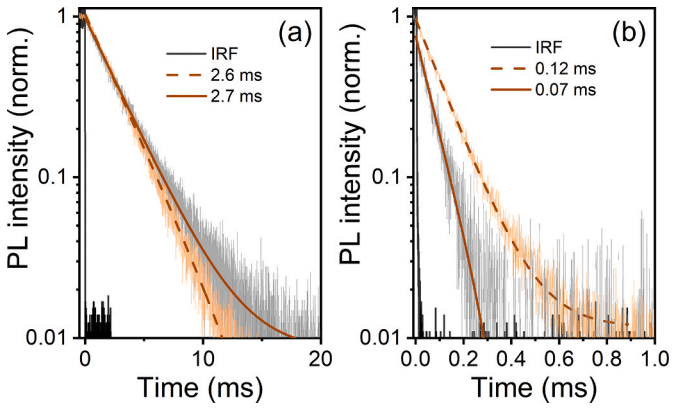

Fig. 5. Luminescence decays of the dried $GdVO_4$:Yb^{3+},Er^{3+},Zn^{2+} sample: (a) decay of the Er^{3+}:$^4I_{13/2}$ state and (b) decay of the Er^{3+}:$^4I_{11/2}$&Yb^{3+}:$^4F_{5/2}$ manifold. Dashed lines correspond to the as-synthesized mixture of microparticles and nanoparticles ($GdVO_4$:Yb^{3+},Er^{3+},Zn^{2+}(16 h) sample), while solid lines correspond to the nanoparticle fraction only ($GdVO_4$:Yb^{3+},Er^{3+},Zn^{2+}(np) sample). IRF – instrument response function of the experimental setup with 976 nm excitation.

The fact that there was an effective quenching of the Er^{3+}:$^4I_{11/2}$&Yb^{3+}:$^4F_{5/2}$ manifold, while the Er^{3+}:$^4I_{13/2}$ state remained unquenched, was rather unexpected. Wang and Meijerink previously reported that energy migration in singly-doped Er^{3+}-doped $NaYF_4$ nanoparticles increased when the Er^{3+} concentration exceeded 10% [34]. This threshold concentration was significantly higher than the Er^{3+} concentration used in this work, but the threshold concentration was comparable to the total concentration of Er^{3+} and Yb^{3+} ions (14 mol %). Thus, it can be assumed that efficient excited state migration between Er^{3+}:$^4I_{11/2}$&Yb^{3+}:$^4F_{5/2}$ manifolds, which is proportional to the total concentration of Yb^{3+} and Er^{3+}, provided an efficient coupling between the Er^{3+}:$^4I_{11/2}$&Yb^{3+}:$^4F_{5/2}$ excited states and the surface quenching centers. Migration between Er^{3+}:$^4I_{13/2}$ excited states and their quenching was less likely due to the lower Er^{3+} ion concentration of only 2 mol %.

It should be noted that in plastic sorting applications, luminescent materials can operate in a humid environment or are dispersed in a media with significant amount of –OH groups, which can thus significantly degrade their luminescence properties. Therefore, the effect of two dispersed media, namely H_2O (strong quenching medium) and D_2O (weak quenching medium), on the SWIR luminescence of the $GdVO_4$:Yb^{3+},Er^{3+},Zn^{2+}(16 h) sample was examined.

3.4. *Quantum yield of $GdVO_4$:Yb^{3+},Er^{3+},Zn^{2+} sample in H_2O and D_2O*

Fig. 6a displays the DRS spectrum of the $GdVO_4$:Yb^{3+},Er^{3+},Zn^{2+}(16 h) sample together with the absorption spectra of H_2O and D_2O in the 900–1000 nm range. When optical excitation at 976 nm is used, water exhibits a significant absorption at this wavelength. Furthermore, Fig. 6b shows the absorption spectra of H_2O and D_2O in the range of 1000–1800 nm as well as the luminescence spectra of the Er^{3+}:$^4I_{13/2}$ state in the $GdVO_4$:Yb^{3+},Er^{3+},Zn^{2+}(16 h) sample. A strong overlap between the luminescence of the Er^{3+}:$^4I_{13/2}$ state and the H_2O absorption spectra was observed. Thus, the aqueous medium can either quench or reabsorb Er^{3+} SWIR radiation, significantly reducing the number of emitted photons reaching the optical detector (in other words, reducing the brightness of the SWIR-luminophore).

In the case of the $GdVO_4$:Yb^{3+},Er^{3+},Zn^{2+}(16 h) sample dispersed in H_2O and D_2O, QY remained high - 2.3% and 11.8% in H_2O and D_2O, respectively. At the same time, the dispersed media decreased the lifetimes of the Er^{3+}:$^4I_{11/2}$&Yb^{3+}:$^4F_{5/2}$ manifold from 0.12 ms in the solid state to 0.09 and 0.10 ms in H_2O and D_2O, respectively (Fig. 7b). The

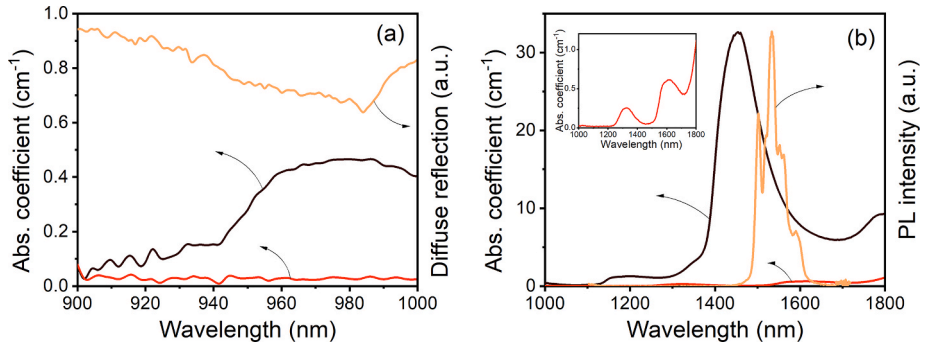

Fig. 6. (a) Absorption spectra of H_2O (black line) and D_2O (red line) in the range of 900–1000 nm and diffuse reflectance spectra of $GdVO_4$:Yb^{3+},Er^{3+},Zn^{2+} powder (orange line); (b) absorption spectra of H_2O (black line) and D_2O (red line) in the range of 1000–1800 nm and emission spectra of $GdVO_4$:Yb^{3+},Er^{3+},Zn^{2+} powder (orange line).

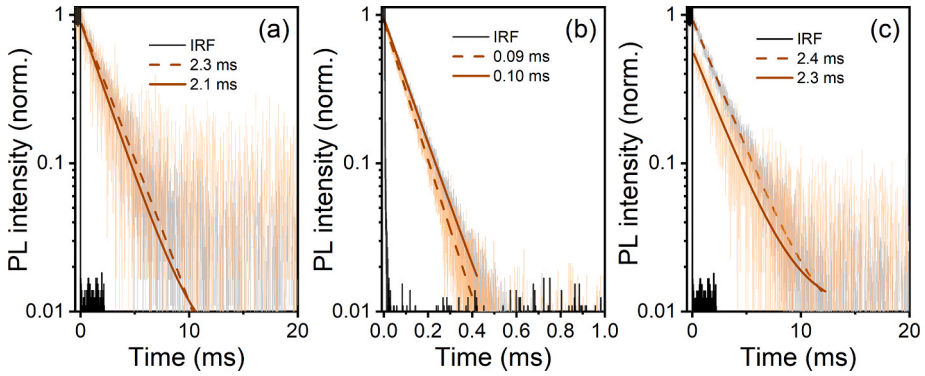

Fig. 7. Luminescence decays of $GdVO_4$:Yb^{3+},Er^{3+},Zn^{2+}(16 h) sample dispersed in H_2O (dashed lines) and D_2O (solid lines); (a) decay of the Er^{3+}:$^4I_{13/2}$ state and (b) decay of the Er^{3+}:$^4I_{11/2}$&Yb^{3+}:$^4F_{5/2}$ manifold, (c) luminescence decay the Er^{3+}:$^4I_{13/2}$ state for the nanoparticles fraction ($GdVO_4$:Yb^{3+},Er^{3+},Zn^{2+}(np) sample) in H_2O. IRF – instrument response function of the experimental setup with 976 nm excitation.

lifetime of the Er^{3+}:$^4I_{13/2}$ state was also slightly reduced as compared to the lifetime in the solid state, and to the same extent in both H_2O and D_2O (Fig. 7a). Although the two dispersed media have very different fundamental vibrational frequencies (D_2O has a characteristic strong peak at 2300-2750 cm ^{1}, while H_2O has a strong peak at 3200-3500 cm ^{1} (see e.g. data from the National Institute of Standards and Technology [43,44]), they have a similarly small effect on the lifetime of the Er^{3+}:$^4I_{11/2}$&Yb^{3+}:$^4F_{5/2}$ manifold and the Er^{3+}:$^4I_{13/2}$ state. Thus, the additional decrease of QY in water can only be explained by the reabsorption of emitted photons by the strong absorption band of H_2O between 1400 nm and 1600 nm.

In contrast, for the $GdVO_4$:Yb^{3+},Er^{3+},Zn^{2+}(np) sample (with a size of 125 nm) in water, QY dropped below a value that can be reliably measured for liquid dispersions (0.1%) although the nanoparticles still exhibit a detectable fraction of the unquenched emission from the Er^{3+}:$^4I_{13/2}$ state with a lifetime of 2.2 ms (Fig. 7c) - the decay showed a very short-lived component with an amplitude of 47% and an unquenched decay component (lifetime of 2.2 ms) with an amplitude of 53%. The very strong quenching of the intermediate state (the Er^{3+}:$^4I_{11/2}$&Yb^{3+}:$^4F_{5/2}$ manifold) was observed, since no luminescence was detected in the range of 1000–1100 nm. These results show that even in the case of relatively large (125 nm) nanoparticles the –OH quenching centers (either on the nanoparticle surface or as part of the chemical structure of the solvent) have a large influence on the quenching of the Er^{3+}:$^4I_{11/2}$&Yb^{3+}:$^4F_{5/2}$ manifold. Therefore, in order to maintain the high QY value for SWIR emission observed for the phosphor in the solid state, it is crucial to avoid interaction of the Er^{3+}:$^4I_{11/2}$&Yb^{3+}:$^4F_{5/2}$ manifold with vibrations of –OH groups.

It should be noted that the QY value of the SWIR emission (1533 nm) of Er^{3+} for crystals dispersed in a solvent is also rarely reported in the literature, while the focus of optical measurements is on the upconversion luminescence in the visible region. As a good exception, Fischer et al. reported the highest QY of 18.55% for a series samples of core-shell β-$NaYF_4$:Yb^{3+}, Er^{3+}@ β-$NaLuF_4$ nanoparticles (core size 23.8 nm) dispersed in chloroform [45]. Tsuboi et al. reported QY of 0.2% for rod-shaped (183 × 113 nm) $NaYF_4$;Yb^{3+}, Er^{3+} nanoparticles dispersed in H_2O [46]. The current work for $GdVO_4$-based materials generally follows the trend described in the aforementioned publications: in –OH–free media, the QY of the SWIR emission (1530 nm) was high, whereas when the nanoparticles were placed in water, there was a significant decrease in the SWIR emission.

4. Conclusions

$GdVO_4$ co-doped with Yb^{3+}, Er^{3+} prepared by high-temperature solid-phase reaction and co-precipitation methods exhibited micrometric and nanometric sizes, respectively. The microparticles from the high-temperature solid-phase method (at T = 1050 °C) showed larger crystallite size, absence of quenching centers (-OH groups) and higher QY (13%) of SWIR luminescence (Er^{3+} luminescence peak at 1533 nm). In contrast, the nanoparticles obtained by the co-precipitation reaction demonstrated small crystallite size, small particle diameter and low QY (0.02%) of the SWIR luminescence. To improve the optical performance of $GdVO_4$ nanoparticles, the addition of Zn^{2+} as a co-dopant ion along with annealing at 700 °C was used so that $GdVO_4$:Yb^{3+}, Er^{3+}, Zn^{2+} demonstrated an increase in QY up to 27.2%. However, a bimodal size distribution (as mixture of nano- and microparticles) was observed in the volume-weighted size distribution after the calcination process. The fraction of small nanoparticles with size of 125 nm was isolated from the $GdVO_4$:Yb^{3+}, Er^{3+}, Zn^{2+} suspension and the QY was found to be

significantly lower (0.9%) than the QY value for the microparticles.

In many potential applications, the dispersing medium can affect the SWIR luminescence characteristics of co-doped $GdVO_4$, both on luminescence lifetime and QY. According to our results, vibrations of the O–H bonds decreased the lifetimes of the Er^{3+}:$^4I_{11/2}$&Yb^{3+}:$^4F_{5/2}$ manifold of $GdVO_4$:Yb^{3+}, Er^{3+}, Zn^{2+} microparticles in H_2O compared to the solid dry sample. At the same time, the lifetime of the Er^{3+}:$^4I_{13/2}$ state remained unchanged. The combination of these lifetime changes resulted in only a slight decrease of QY of the microparticles dispersed in H_2O. In contrast, the QY of 125 nm $GdVO_4$:Yb^{3+}, Er^{3+}, Zn^{2+} nanoparticles in water phase decreased dramatically (QY $<$ 0.1%) due to extremely efficient quenching of the Er^{3+}:$^4I_{11/2}$&Yb^{3+}:$^4F_{5/2}$ manifold by O–H bond vibrations. Therefore, an additional protection strategy is required to improve the efficiency of SWIR luminescence even in relatively large (125 nm) $GdVO_4$ nanoparticles.

Overall, $GdVO_4$:Yb^{3+}, Er^{3+}microparticles with QY of 27.2% in the SWIR region demonstrate a potential of using as luminescent markers for Tracer-Based Sorting – a new technology in plastics recycling.

Associated content

The Supporting Information is available free of charge.

Notes

There are no conflicts of interest to declare.

CRediT authorship contribution statement

Yupaporn Niyom: Conceptualization, Methodology, Investigation, Formal analysis, Validation, Writing – original draft, Writing - Full Draft. **Eduard Madirov:** Methodology, Investigation, Formal analysis, Validation. **Nisrin Mohamed Bhiri:** Methodology, Investigation, Formal analysis, Validation. **Aditya Chauhan:** Methodology, Investigation, Formal analysis, Validation. **Bryce S. Richards:** Supervision, Funding acquisition, Resources, Writing – review & editing. **Adrian Flood:** Conceptualization, Funding acquisition, Resources, Supervision, Writing – review & editing. **Daniel Crespy:** Conceptualization, Funding acquisition, Resources, Supervision, Writing – review & editing. **Andrey Turshatov:** Conceptualization, Funding acquisition, Resources, Visualization, Supervision, Project administration, Writing – review & editing.

Declaration of competing interest

The authors declare the following financial interests/personal relationships which may be considered as potential competing interests: Yupaporn Niyom reports financial support was provided by Vidyasirimedhi Institute of Science and Technology (VISTEC). Adrian Flood reports financial support was provided by Vidyasirimedhi Institute of Science and Technology (VISTEC). Daniel Crespy reports financial support was provided by Vidyasirimedhi Institute of Science and Technology (VISTEC). Bryce Richards reports financial support was provided by Helmholtz Association of German Research Centers. Bryce Richards reports financial support was provided by European Commission. Andrey Turshatov reports financial support was provided by European Commission.

Data availability

Data will be made available on request.

Acknowledgment

Y.N., A.F., D.C. acknowledges Vidyasirimedhi Institute of Science and Technology (VISTEC) for financial support. The financial support provided by the Helmholtz Association is gratefully acknowledged: (i) a Recruitment Initiative Fellowship for B.S.R.; (ii) the funding of chemical synthesis equipment from the Helmholtz Materials Energy Foundry (HEMF); and (iii) Research Field Energy – Program Materials and Technologies for the Energy Transition – Topic 1 Photovoltaics. A.C., B. S.R. and A.T. acknowledge funding from the European Union's Horizon 2020 research and innovation project "Circular Foodpack" agreement No: 101003806.

References

[1] W. Tao, O.C. Farokhzad, Chem. Rev. 122 (2022) 5405–5407.
[2] Y. Liu, Y. Li, S. Koo, Y. Sun, Y. Liu, X. Liu, Y. Pan, Z. Zhang, M. Du, S. Lu, X. Qiao, J. Gao, X. Wang, Z. Deng, X. Meng, Y. Xiao, J.S. Kim, X. Hong, Chem. Rev. 122 (2022) 209–268.
[3] M. Tan, F. Li, X. Wang, R. Fan, G. Chen, ACS Nano 14 (2020) 6532–6538.
[4] J. Woidasky, I. Sander, A. Schau, J. Moesslein, P. Wendler, D. Wacker, G. Gao, D. Kirchenbauer, V. Kumar, D. Busko, I.A. Howard, B.S. Richards, A. Turshatov, S. Wiethoff, C. Lang-Koetz, Resour. Conserv. Recycl. 161 (2020), 104976.
[5] J. Gasde, J. Woidasky, J. Moesslein, C. Lang-Koetz, Sustainability 13 (2021) 258.
[6] X. Wu, J. Li, L. Yao, Z. Xu, J. Clean. Prod. 246 (2020), 118732.
[7] J. Li, Y. Dong, R. Wei, G. Jiang, C. Yao, M. Lv, Y. Wu, S.H. Gardner, F. Zhang, M. Y. Lucero, J. Huang, H. Chen, G. Ge, J. Chan, J. Chen, H. Sun, X. Luo, X. Qian, Y. Yang, J. Am. Chem. Soc. 144 (2022) 14351–14362.
[8] J. Qi, C. Sun, A. Zebibula, H. Zhang, R.T.K. Kwok, X. Zhao, W. Xi, J.W.Y. Lam, J. Qian, B.Z. Tang, Adv. Mater. 30 (2018), 1706856.
[9] H. Piwoński, W. Li, Y. Wang, T. Michinobu, S. Habuchi, ACS Applied Polymer Materials 2 (2020) 569–577.
[10] H. Piwoński, S. Nozue, S. Habuchi, ACS Nanoscience Au 2 (2022) 253–283.
[11] H. Piwoński, Y. Wang, W. Li, T. Michinobu, S. Habuchi, Nano Lett. 20 (2020) 8803–8810.
[12] Y. Zhong, Z. Ma, F. Wang, X. Wang, Y. Yang, Y. Liu, X. Zhao, J. Li, H. Du, M. Zhang, Q. Cui, S. Zhu, Q. Sun, H. Wan, Y. Tian, Q. Liu, W. Wang, K.C. Garcia, H. Dai, Nat. Biotechnol. 37 (2019) 1322–1331.
[13] E. Thimsen, B. Sadtler, M.Y. Berezin, Nanophotonics 6 (2017) 1043–1054.
[14] H. Yu, J. Liu, H. Zhang, A.A. Kaminskii, Z. Wang, J. Wang, Laser Photon. Rev. 8 (2014) 847–864.
[15] M. Abdesselem, M. Schoeffel, I. Maurin, R. Ramodiharilafy, G. Autret, O. Clément, P.-L. Tharaux, J.-P. Boilot, T. Gacoin, C. Bouzigues, A. Alexandrou, ACS Nano 8 (2014) 11126–11137.
[16] P.C. de Sousa Filho, J. Alain, G. Leménager, E. Larquet, J. Fick, A.S. Osvaldo, T. Gacoin, J. Phys. Chem. C 123 (2019) 2441–2450.
[17] A. Huignard, T. Gacoin, J.-P. Boilot, Chem. Mater. 12 (2000) 1090–1094.
[18] A. Huignard, V. Buissette, G. Laurent, T. Gacoin, J.P. Boilot, Chem. Mater. 14 (2002) 2264–2269.
[19] M. Toro-González, R. Copping, S. Mirzadeh, J.V. Rojas, J. Mater. Chem. B 6 (2018) 7985–7997.
[20] Z. Lv, L. Jin, Y. Cao, H. Zhang, D. Xue, N. Yin, T. Zhang, Y. Wang, J. Liu, X. Liu, H. Zhang, Light Sci. Appl. 11 (2022) 116.
[21] A. Chauhan, S. Kataria, D. Busko, F.A. Cardona, A. Turshatov, B.S. Richards, J. Mater. Chem. C 9 (2021) 16709–16720.
[22] K. Keevend, L. Puust, K. Kurvits, L.R.H. Gerken, F.H.L. Starsich, J.-H. Li, M. T. Matter, A. Spyrogianni, G.A. Sotiriou, M. Stiefel, I.K. Herrmann, Nano Lett. 19 (2019) 6013–6018.
[23] Z. Xu, X. Kang, C. Li, Z. Hou, C. Zhang, D. Yang, G. Li, J. Lin, Inorg. Chem. 49 (2010) 6706–6715.
[24] A. Szczeszak, T. Grzyb, Z. Śniadecki, N. Andrzejewska, S. Lis, M. Matczak, G. Nowaczyk, S. Jurga, B. Idzikowski, Inorg. Chem. 53 (2014) 12243–12252.
[25] Y.-C. Chen, Y.-C. Wu, D.-Y. Wang, T.-M. Chen, J. Mater. Chem. 22 (2012) 7961–7969.
[26] N.S. Singh, R.S. Ningthoujam, M.N. Luwang, S.D. Singh, R.K. Vatsa, Chem. Phys. Lett. 480 (2009) 237–242.
[27] A. Huignard, V. Buissette, A.-C. Franville, T. Gacoin, J.-P. Boilot, J. Phys. Chem. B 107 (2003) 6754–6759.
[28] N.S. Singh, R.S. Ningthoujam, L.R. Devi, N. Yaiphaba, V. Sudarsan, S.D. Singh, R. K. Vatsa, R. Tewari, J. Appl. Phys. 104 (2008).
[29] W. Yin, L. Zhou, Z. Gu, G. Tian, S. Jin, L. Yan, X. Liu, G. Xing, W. Ren, F. Liu, Z. Pan, Y. Zhao, J. Mater. Chem. 22 (2012) 6974–6981.
[30] G. Mialon, S. Türkcan, G. Dantelle, D.P. Collins, M. Hadjipanayi, R.A. Taylor, T. Gacoin, A. Alexandrou, J.-P. Boilot, J. Phys. Chem. C 114 (2010) 22449–22454.
[31] V. Mahalingam, C. Hazra, R. Naccache, F. Vetrone, J.A. Capobianco, J. Mater. Chem. C 1 (2013) 6536–6540.
[32] R.E. Joseph, C. Jiménez, D. Hudry, G. Gao, D. Busko, D. Biner, A. Turshatov, K. Krämer, B.S. Richards, I.A. Howard, J. Phys. Chem. 123 (2019) 6799–6811.
[33] B. Grunert, J. Saatz, K. Hoffmann, F. Appler, D. Lubjuhn, N. Jakubowski, U. Resch-Genger, F. Emmerling, A. Briel, ACS Biomater. Sci. Eng. 4 (2018) 3578–3587.
[34] Z. Wang, A. Meijerink, J. Phys. Chem. C 122 (2018) 26298–26306.

[35] B. Huang, J. Bergstrand, S. Duan, Q. Zhan, J. Widengren, H. Ågren, H. Liu, ACS Nano 12 (2018) 10572–10575.
[36] J.T. Vega-Durán, O. Barbosa-García, L.A. Diáz-Torres, M.A. Meneses-Nava, D. S. Sumida, Appl. Phys. Lett. 76 (2000) 2032–2034.
[37] J. García-Sevillano, E. Cantelar, A. Justo, M. Ocaña, F. Cussó, Mater. Chem. Phys. 138 (2013) 666–671.
[38] S.N.B. Bhaktha, B. Boulard, S. Chaussedent, A. Chiappini, A. Chiasera, E. Duval, C. Duverger, S. Etienne, M. Ferrari, Y. Jestin, M. Mattarelli, M. Montagna, A. Monteil, E. Moser, H. Portales, K.C. Vishunubhatla, Opt. Mater. 28 (2006) 1325–1328.
[39] F. Artizzu, M. Atzori, J. Liu, D. Mara, K. Van Hecke, R. Van Deun, J. Mater. Chem. C 7 (2019) 11207–11214.
[40] M. Zhang, W. Zheng, Y. Liu, P. Huang, Z. Gong, J. Wei, Y. Gao, S. Zhou, X. Li, X. Chen, Angew. Chem. Int. Ed. 58 (2019) 9556–9560.
[41] Y. Pei, D. Tu, C. Li, S. Han, Z. Xie, F. Wen, L. Wang, X. Chen, Angew. Chem. Int. Ed. 61 (2022), e202205276.
[42] J. Sun, W. Zheng, P. Huang, M. Zhang, W. Zhang, Z. Deng, S. Yu, M. Jin, X. Chen, Angew. Chem. Int. Ed. 61 (2022), e202201993.
[43] https://webbook.nist.gov/cgi/cbook.cgi?ID=C7732185&Type=IR-SPEC&Index=1.
[44] https://webbook.nist.gov/cgi/cbook.cgi?ID=B6010117&Mask=80.
[45] S. Fischer, N.D. Bronstein, J.K. Swabeck, E.M. Chan, A.P. Alivisatos, Nano Lett. 16 (2016) 7241–7247.
[46] S. Tsuboi, S. Yamada, Y. Nakane, T. Sakata, H. Yasuda, T. Jin, ECS Journal of Solid State Science and Technology 7 (2017) R3093–R3101.